Crystallization in the Vesicle Walls Templated by Dry-Brush Block Copolymer/Homopolymer Blend

Hsin-Lung Chen,*,† Shih-Yueh Lin,† Yen-Yu Huang,† Fang-Chyou Chiu,‡ Willisa Liou,§ and J. S. Lin⊥

Department of Chemical Engineering, National Tsing Hua University, Hsin-Chu, Taiwan 30013, R.O.C.; Department of Chemical and Materials Engineering, Chang Gung University, Kwei-San, Taoyuan, 333, Taiwan, R.O.C.; Department of Anatomy, Chang Gung University, Kwei-San, Taoyuan, 333, Taiwan, R.O.C.; and Solid State Division, Oak Ridge National Laboratory, Oak Ridge, Tennessee 37831

Received June 25, 2002; Revised Manuscript Received October 3, 2002

ABSTRACT: We studied the crystallization behavior in a diblock copolymer/homopolymer blend system exhibiting "dry-brush" phase behavior in the melt. A nearly symmetric poly(ethylene oxide)-*block*-polybutadiene (PEO-*b*-PB) was blended with a PB homopolymer (h-PB) having approximately the same molecular weight as that of the PB block, thereby yielding the dry-brush blends wherein h-PB was localized in the PB microdomain, causing expansion of PB domain thickness without introducing transformation in microdomain morphology. Even though the lamellar identity of PEO domain retained throughout the blend composition, the lamellar units became increasingly isolated as characterized by the formations of cylindrical and spherical vesicles at high h-PB compositions. Over the major composition range ($w_{h-PB} \leq 0.7$), crystallization of PEO blocks in the vesicle wall was able to take place at the undercooling comparable to that of PEO homopolymer, implying that the crystallization mechanism was analogous to the homopolymer crystallization initiated predominantly through heterogeneous nucleation followed by long-range crystal growth. At the compositions ($w_{h-PB} \geq 0.8$) where most PEO lamellae formed shells of spherical vesicles in the melt, the crystallization was effectively confined within the individual vesicle, and it only occurred at very deep undercooling ($\Delta T > 70$ K). The corresponding isothermal crystallization followed the first-order kinetics prescribed by a nucleation-controlled crystallization wherein the crystallization started from homogeneous nuclei followed by essentially instantaneous crystal growth to fill the vesicle wall. In general, the confinement effect exerted by dry-brush blending was far less effective than the corresponding wet-brush blending.

Introduction

Crystalline−amorphous (C−A) diblock copolymers exhibit complex structural patterns due to combined effect of crystallization and microphase separation. When the two components are of similar proportion or when C block becomes the minor constituent, microphase separation in the melt may generate a series of long-range ordered microdomains (e.g., lamellae, cylinder, or sphere) consisting of C blocks. Studies of crystallization within these nanoscaled domains can facilitate understandings on the crystallization behavior of chain molecules under spatial confinement. Recent studies have revealed the crystal orientation (with respect to microdomain interface),[1−9] crystallization kinetics,[7,10−27] and the resultant crystalline morphology[15,16,21,24,28−32] of C−A diblock copolymers. Microdomain geometry,[20,21,23,26,27,33] strength of interblock repulsion,[24,26,34−36] and T_g of the amorphous phase (T_g^A)[7,22,30,37] are considered as the major parameters that control the kinetics and thermodynamics associated with the structural formation.

In the case where T_g^A lies below the crystallization temperature (T_c), the melt structure may be perturbed by crystallization in the microdomains.[15,16,21,24,29,32] The capacity of the crystallization driving force to perturb the melt structure can have strong impact on the crystallization kinetics.[15,20,21,23,24,26] On the basis of the extent of structural perturbation and the corresponding kinetics pattern, Loo et al. classified the crystallization mechanism into three modes, namely, breakout, templated, and confined.[24] Breakout and templated crystallizations can take place at the normal undercooling (i.e., the undercooling comparable to that of the homopolymer) because the processes are predominantly initiated by heterogeneous nucleation followed by long-range crystal growth. Extended crystal growth in breakout mode is driven by the capability of the crystallization driving force to disrupt the melt structure, while that in the templated process may be assisted by the inherent connectivity of microdomains in the melt or by short-range intrusion of growth front into the nearby domains.[24,38] Isothermal crystallization in both modes yields sigmoidal crystallinity development closely described by the classical Avrami theory.[21,23,24] Confined crystallization may be defined as the case where the crystallization is totally restricted within the individual domains. Melt morphology largely retains in this case, and crystallization within the majority of domains has to be initiated by homogeneous nucleation because the microdomains outnumber the heterogeneous nuclei significantly.[19,23−26] Exceedingly large undercooling is required to promote these nucleation events, and the development of crystallinity during isothermal crystallization follows the first-order kinetics prescribed by a nucleation-controlled process wherein the crystallization starts from homogeneous nuclei followed by essentially

† National Tsing Hua University.
‡ Department of Chemical and Materials Engineering, Chang Gung University.
§ Department of Anatomy, Chang Gung University
⊥ Oak Ridge National Laboratory.
* To whom correspondence should be addressed.

10.1021/ma020997l CCC: $22.00
Published on Web 11/05/2002

instantaneous crystal growth to fill the domain space.[19,21,23,24,27]

Since different domain geometries may exert different degrees of spatial confinement to the crystallization process, the crystallization mode in diblock copolymers should depend heavily on microdomain morphology. To reveal the effect of domain geometry, it is essential to compare the crystallization behavior among different types of microdomains surrounded by identical amorphous matrix while keeping the molecular weight of C block fixed. The most convenient approach to achieve such a sample requirement is probably through blending a C−A diblock copolymer with A homopolymer (h−A), because the uniform solubilization of h−A in A microdomains is capable of inducing morphological transformation from, say, C lamellae to C cylinders to C spheres, while maintaining the molecular weight of C block throughout.[39−41]

In the previous studies, we investigated crystallization in the blends of a symmetric poly(ethylene oxide)-*block*-polybutadiene (PEO-*b*-PB) with a low molecular weight PB homopolymer (h-PB).[20,21] The freezing temperature (T_f) of PEO determined from the DSC cooling experiment was found to display distinct transitions at the compositions corresponding to the morphological transformation, and the undercoolings required to initiate crystallizations in cylindrical and spherical morphlologies were much larger than that associated with lamellar melt due to homogeneous nucleation-controlled mechanism. A recent study by Xu et al. demonstrated that different modes of T_f−composition plots can be obtained in PEO-*block*-poly(oxybutylene)/poly(oxybutylene) blends depending upon the segregation strengths prescribed by the block lengths.[26]

It should be noted that the diblock blends discussed above are called "wet-brush" systems, wherein the molecular weight of h-A (M_{h-A}) is smaller than that of A block (M_{b-A}), i.e., $\alpha = M_{h-A}/M_{b-A} < 1$.[40] Another type of diblock copolymer blends called "dry brush" is formed by blending with h-A having nearly the same molecular weight as that of A block, i.e., $\alpha \approx 1$.[40,42,43] In this case, h-A may still enter into A microdomains, but the homopolymer chains are localized at the mid or core regions of the domains. Such a dry-brush pattern only causes swelling of A domain thickness but not transformation of domain morphology. For instance, when a lamellae-forming C−A diblock is blended with h-A to form dry-brush blends, the thickness of A domains can be swollen continuously while keeping the lamellar identity and thickness of C domains; therefore, this type of system offers an interesting model for studying the crystallization in lamellar phase with a broad range of interlamellar separation. Moreover, the global structure of the lamellar units may form cylindrical or spherical vesicles at high h-A compositions with the vesicle walls composed of C blocks.[42,44] These vesicle structures constitute special geometric confinement not offered by the classical microdomain patterns to the crystallization process. Effects of such types of spatial confinement, to our knowledge, have not been explored.

In this study, we investigate the crystallization behavior in the dry-brush blends of PEO-*b*-PB and h-PB. A lamellae-forming PEO-*b*-PB was blended with a h-PB having approximately the same molecular weight as that of PB block, thereby yielding the dry-brush PEO-*b*-PB/h-PB blends. The crystallization of PEO blocks within the lamellar microdomains is studied as a function of h-PB composition. It will be shown that, in contrast to the corresponding wet-brush blends, crystallization in the dry-brush system can proceed at the normal undercooling over the major composition range. At very high h-PB composition where the PEO lamellae in the melt are highly isolated due to formation of spherical vesicles, crystallization becomes a homogeneous nucleation-controlled process.

Experimental Section

PEO-*b*-PB with the polydispersity index (M_w/M_n) of 1.04 was synthesized by sequential anionic polymerization of butadiene and ethylene oxide (Polymer Source, Inc.). The molecular weights according to the supplier were $M_{n,b-PEO} = 43\,500$ and $M_{n,b-PB} = 32\,000$, which prescribed the volume fraction of PEO (f_{PEO}) = 0.54. The 1,4-addition h-PB used for dry-brush blending had $M_n = 35\,000$ ($\alpha = 1.1$) and $M_w/M_n = 1.05$. Microphase-separated blends were prepared by solution mixing using toluene as the cosolvent, followed by removing the solvent in vacuo at 80 °C. The blend composition was expressed in terms of the weight fraction of h-PB, w_{h-PB}.

SAXS was utilized to probe the morphology in the melt and crystalline state. For the study of melt morphology, SAXS measurements were performed at 90 °C ($T_m^{PEO} < 90$ °C $< T_{ODT}$) to avoid PEO crystallization. As for the characterization of crystalline morphology, the samples were prepared by quench from 90 to 27 °C or from 90 °C into liquid nitrogen. The ultimate crystallinity in terms of the weight of crystals per unit weight of PEO was over 0.65 irrespective of blend composition and crystallization history. SAXS characterizations of all crystalline samples were conducted at room temperature. The SAXS apparatus consisted of an 18 kW rotating-anode X-ray generator operated at 40 kV × 200 mA (Rigaku), a graphite crystal for incident beam monochromatization, and a two-dimensional position-sensitive detector (ORDELA model 2201X, Oak Ridge Detector Laboratory Inc.). The intensity profiles were output as the plot of scattering intensity (I) vs scattering vector, $q = (4\pi/\lambda)\sin(\theta/2)$ (θ = scattering angle). Details of the SAXS setup have been described elsewhere.[21]

Crystallization kinetics was studied by the fixed cooling rate and isothermal crystallization experiments in a TA Instrument 2000 DSC equipped with the RCS cooling system. For the fixed cooling rate experiment, the sample was first annealed at 90 °C for 5 min and then cooled to −60 °C at a rate of 5 °C/min for the recording of the crystallization exotherms. The temporal development of crystallinity was monitored in the isothermal crystallization experiment following the procedure described in our previous study.[21]

The real-space morphology of the blends was observed at room temperature by a JEOL JEM-2000FXZ transmission electron microscope operated at 120 kV. The film specimens were microtomed at −90 °C, using a Reichert Ultracut E low-temperature sectioning system. The ultrathin sections were stained with the vapor of 1% OsO_4(aq) for 1 h.

Results and Discussion

Melt Morphology. The microphase-separated morphology of the blends in the melt was probed by SAXS to verify the dry-brush phase behavior. Figure 1 displays the Lorentz-corected SAXS profiles (Iq^2 vs q) collected at 90 °C. Neat PEO-*b*-PB shows well-defined lattice peaks with relative positions (1:2:3:...) closely relevant to lamellar morphology. The interlamellar distance calculated from the primary peak position ($L = 2\pi/q_m$) is 65.5 nm. The thickness of PEO lamellae (L_{PEO}) is therefore 35.4 nm, considering the volume fraction of PEO is 0.54.

Upon addition of h-PB, the lattice peaks shift toward lower q and broaden due to increases in L and breadth of distribution of L (σ_L) arising from local solubilization

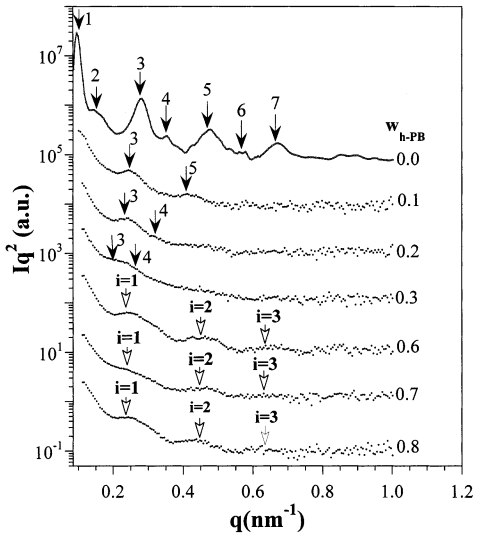

Figure 1. Lorentz-corrected SAXS profiles of dry-brush PEO-*b*-PB/h-PB blends in the melt. The SAXS experiments were conducted at 90 °C (T_m < 90 °C < T_{ODT}). The lattice peaks are marked by the solid arrows, whereas the maxima denoted by "$i = n$" (n = 1, 2, 3) are associated with the form factor scattering from individual PEO lamellae.

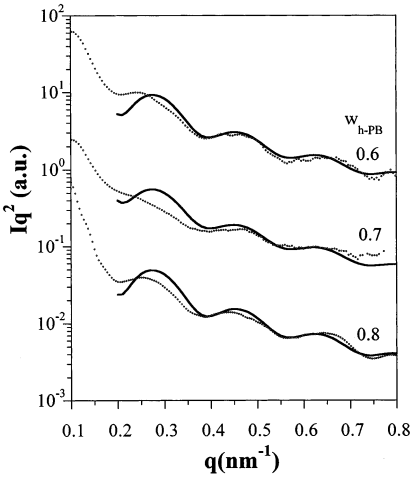

Figure 2. Fits of the observed form factor scattering of dry-brush PEO-*b*-PB/h-PB blends by the lamellar form factor. The solid curves are the calculated profiles. The average thickness of PEO lamellae ($\langle L_{PEO}\rangle$) and the standard deviation of L_{PEO} (σ_{PEO}) obtained from the fit are (a) $w_{h-PB} = 0.6$: $\langle L_{PEO}\rangle = 35.4$ nm, $\sigma_{PEO} = 8.0$ nm; (b) $w_{h-PB} = 0.7$: $\langle L_{PEO}\rangle = 36.0$ nm, $\sigma_{PEO} = 9.4$ nm; and (c) $w_{h-PB} = 0.8$: $\langle L_{PEO}\rangle = 36.3$ nm, $\sigma_{PEO} = 7.6$ nm.

of h-PB in PB domains. The primary maxima of the blends are located near the beamstop and hence undetectable by our SAXS instrument. Three broad maxima denoted by "$i = n$" (n = 1, 2, 3) observed for $w_{h-PB} \geq 0.6$ are attributed to the form factor scattering from individual PEO lamellae. The observed form factor profiles were fitted by theoretical lamellar form factor with assumption of Gaussian distribution of lamellar thickness,[42] as shown in Figure 2. The calculated profiles closely match the observed ones, and the average lamellar thickness obtained (specified in the caption of Figure 2) agrees with 35.4 nm calculated from L of the neat diblock. Therefore, the lamellar identity and thickness of PEO microdomains are essentially unperturbed upon blending, a typical feature of dry-brush blend.

Even though the lamellar identity of PEO domain retains throughout the blend composition, the global structure of the lamellar unit, called "vesicle", may

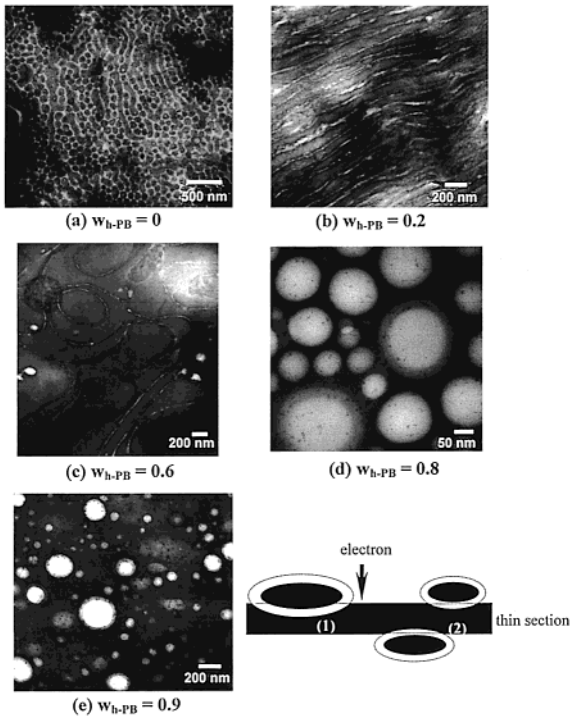

Figure 3. TEM micrographs showing the morphology of dry-brush PEO-*b*-PB/h-PB blends at room temperature (ca. 27 °C). The blend compositions are indicated in the figure. The schematic plot shows the cases which might give rise to the core−shell image (case 1) or image resembling that of simple spheres (case 2) from spherical vesicles.

exhibit different interfacial curvatures depending upon w_{h-PB}. Hashimoto et al. found through a TEM study that the lamellar structure in a dry-brush PS-*b*-PI/h-PS tended to transform from lamellar to cylindrical to spherical vesicles with increasing h-PS composition.[42] It should be noted that resolving the melt structure through room temperature TEM experiment is impossible for the present system, because PEO blocks crystallize at room temperature over the major composition range (to be detailed later). Nevertheless, the morphology observed by TEM may still closely reflect the melt structure if crystallization does not completely disrupt the vesicle structure in the melt.

Figure 3 presents a series of TEM micrographs of the blends. The dark regions correspond to the PB phase owing to preferential staining by OsO_4. It is interesting that neat diblock displays a perforated lamellar morphology (Figure 3a) characterized by highly interconnected PEO lamellae. Since the SAXS profile of the neat diblock collected in situ at 90 °C (Figure 1) suggests a 1-D stacked lamellar structure in the melt state, it may be speculated that crystallization at room temperature tends to break out the lamellar stacks to allow extended crystal growth and eventually leads to interconnected crystalline lamellae. However, considering that only occasional interdomain connection would be necessary to generate extended crystal growth, the highly interconnected lamellae observed is not likely to arise from crystallization alone. Formation of the perforated lamellae, as found in a number of diblock systems in the melt state,[45,46] might be driven by the tendency toward a more stable melt structure upon cooling; however, the exact driving force requires further study.

The lamellar perforation disappears upon addition of h-PB, as the blend with $w_{h-PB} = 0.2$ is found to display

regular lamellar stacking with rather bended interface (Figure 3b). The lamellar stacking is lost when w_{h-PB} is increased to 0.6, as shown in Figure 3c. The lamellae are now wormlike and become increasingly isolated, as some lamellae even form closed loops. The close-looped lamellae may be represented by "cylindrical vesicles", and their formation may arise from the incoherent lamellar bending which increases the probability of one PEO lamellae to intersect itself by thermal activation.[42]

Further addition of h-PB to $w_{h-PB} = 0.8$ transforms the characteristic morphological identity into ellipsoidal or spherical objects, as demonstrated in Figure 3d,e. The large spherical objects with diameters of ca. 150−320 nm display "core−shell" pattern with thickness of the gray coronal shell of ca. 30 nm. The sizes of most spherical objects significantly exceed that of the spherical domains (average diameter = 28 nm) found in the corresponding wet-brush blends. Moreover, the entire form factor profile observed for $w_{h-PB} = 0.8$ in Figure 1 cannot be fitted by the form factor scattering of spheres with uniform electron density, not mentioning that the radius calculated from the position of the first form factor maximum is only 24 nm (much smaller than the average radius observed in Figure 3d,e) if we assume that the observed form factor profile is associated with spheres. Consequently, the spherical objects observed cannot be considered as simple spherical microdomains. We attribute these objects to spherical vesicles consisting of PB core and PEO shell. The diameters of these vesicles exceed the thickness of the thin section, such that the 2-D projection of the sliced cross section may give rise to the core−shell image (as depicted in (1) of the schematic plot in Figure 3, where less than half of the vesicle volume remains in the thin section) or the image resembling that of simple spheres (as depicted in (2) of the scheme) depending upon the portion contained in the thin section.

In light of the SAXS and TEM results, we conclude that the PEO domains retain lamellar identity locally, but the lamellar units become increasingly isolated at high w_{h-PB}, as characterized by the formation of cylindrical or spherical vesicles. Since the composition dependence of the morphology observed follows that of dry-brush PS-*b*-PI/h-PS whose morphology is not complicated by crystallization, we assert that the vesicle structure in the melt was not perturbed significantly by crystallization (at least for the blends), such that the morphological features observed in Figure 3 closely reflect the original melt structures.

Kinetics of Crystallization. The foregoing morphological study indicates that the present blend can serve as an interesting model system for examining the crystallization in a variety of vesicle structures. The crystallization kinetics can be readily evaluated from the fixed cooling rate experiments in the DSC. Figure 4 shows the DSC cooling curves of the blends, while the corresponding T_f (i.e., peak temperature of exotherm) is plotted as a function of w_{h-PB} in the inset. The T_f−composition plot is different from that of the corresponding wet-brush blend showing microdomain-tailored kinetics pattern.[20,21] A crystallization exotherm at ca. 38 °C is observed over the major composition range ($w_{h-PB} \leq 0.7$), implying that the crystallization mechanism was analogous to the homopolymer crystallization (T_f of h-PEO = 39 °C). To reveal the crystallization mechanism in further details, the isothermal crystallization experiments at 47 °C were conducted to identify

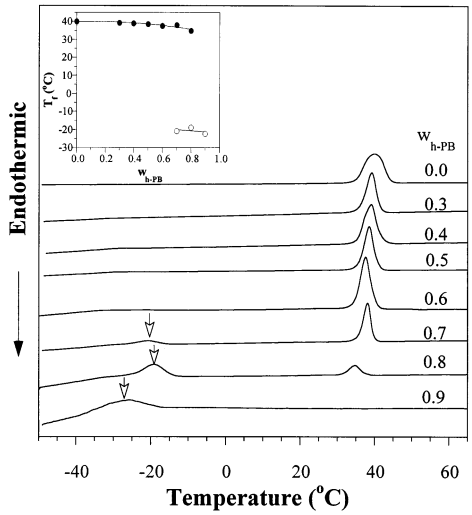

Figure 4. DSC cooling curves of dry-brush PEO-*b*-PB/h-PB blends. The samples were cooled from 90 to −50 °C at −5 °C/min. The low-temperature exotherm which starts to emerge at $w_{h-PB} = 0.7$ is indicated by the opened arrows. The DSC signals have been normalized by the weight fraction of PEO. The inset in the figure shows the freezing temperature (T_f) as a function of w_{h-PB}.

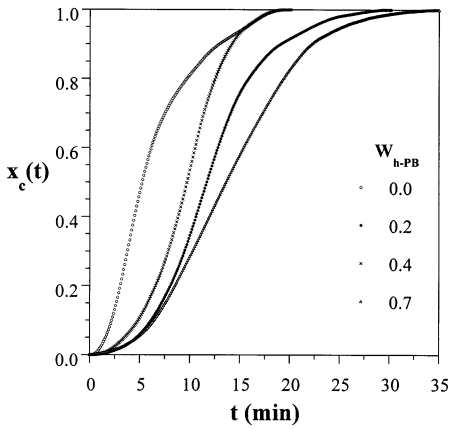

Figure 5. Crystallization isotherms represented by $x_c(t)$ vs t plots of dry-brush PEO-*b*-PB/h-PB blends with $w_{h-PB} \leq 0.7$. The crystallization was conducted at 47 °C. It can be seen that the curves are sigmoidal.

the pattern of crystallinity development. The representative $x_c(t)$ plots are shown in Figure 5. The curves show sigmoidal shape properly described by the Avrami equation with Avrami exponents of 2−3.[47] This is in parallel with the typical homopolymer crystallization initiated predominantly through heterogeneous nucleation followed by a series of long-range crystal growth.

The mechanism of long-range crystal growth may be discussed in light of the morphology observed in Figure 3. If the perforated lamellar structure represents the melt morphology in neat PEO-*b*-PB, extended crystal growth would be facile because of the extensive interlamellar connectivity. In the blends exhibiting regularly stacked lamellae, the connectivity of PEO domains across the grain boundary should be responsible for the extended crystal growth from heterogeneous nuclei without disrupting the melt structure.[23,38] Both cases belong to the templated mode of crystallization.

We now examine the crystallization behavior at high h-PB composition ($w_{h-PB} \geq 0.7$). It can be seen from Figure 4 that an exotherm at −21 °C emerges and coexists with the high-temperature exotherm for w_{h-PB}

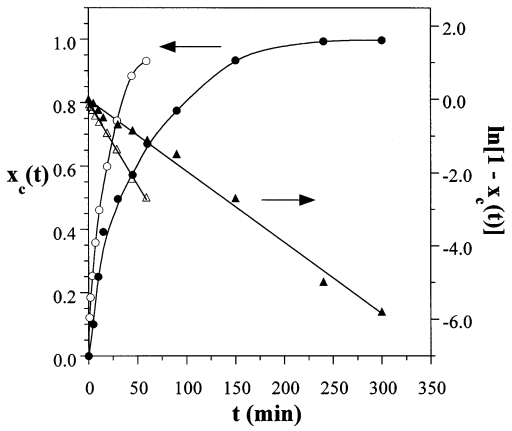

Figure 6. Development of crystallinity in dry-brush PEO-*b*-PB/h-PB blends with $w_{h-PB} = 0.8$ ($T_c = -16$ °C) and 0.9 ($T_c = -24$ °C). Opened and closed symbols present the plots for $w_{h-PB} = 0.8$ amd 0.9, respectively. The curves can be described by the first-order kinetics, as manifested from the linearity of ln-$[1 - x_c(t)]$ vs t plot.

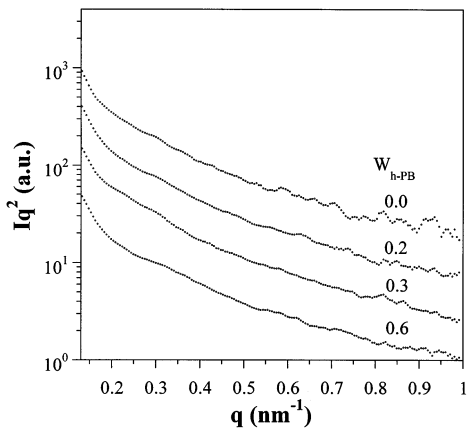

Figure 7. Lorentz-corrected SAXS profiles of dry-brush PEO-*b*-PB/h-PB blends crystallized at 27 °C.

= 0.7. The low-temperature exotherm dominates the high-temperature one as w_{h-PB} is increased to 0.8, and the high-temperature exotherm totally vanishes with further addition of h-PB to $w_{h-PB} = 0.9$. The large underocooling associated with the low-temperature exotherm is attributed to the homogeneous nucleation-controlled crystallization,[11,20,21,25,26] wherein the process is largely confined within highly isolated PEO lamellae. As a matter of fact, the compositions ($w_{h-PB} \geq 0.8$) at which the low-temperature exotherm becomes dominant correspond to those forming spherical vesicles in the melt (Figure 3). Considering that the radius of the largest spherical vesicle is about 150 nm and the PEO shell (lamellae) is about 35 nm thick, the number density of the PEO domains in the melt can be estimated to be $>10^{14}$ cm^{-3}. Because this considerably exceeds the typical density of heterogeneous nuclei in PEO (ca. 10^6 cm^{-3}),[25] crystallizations within the majority of vesicle walls have to proceed through homogeneous nucleation whose occurrence requires very large undercooling.

Isothermal crystallization experiment was also conducted to verify the homogeneous nucleation-controlled mechanism in the compositions exhibiting spherical vesicles in the melt. In the microphase-separated melt where crystallization is effectively confined within the microdomains, it can be assumed that once a nucleus is formed the subsequent crystal growth is essentially instantaneous to fill the domain space.[19,21] This assumption is particularly sound when the nucleation mechanism is homogeneous, since this type of nucleation occurs at very deep undercooling which imparts very large driving force to the secondary nucleation involved in the growth and consequently leads to extremely fast crystal growth. The development of crystallinity for such a nucleation-controlled process is properly described by the first-order kinetics which prescribes the following formula for $x_c(t)$[19,21,23]

$$x_c(t) = 1 - \exp(-k_N t) \qquad (1)$$

where k_N is the nucleation rate constant. Figure 6 displays the representative $x_c(t)$ plots for the blends with $w_{h-PB} = 0.8$ and 0.9 crystallized at $T_c = -16$ and -24 °C, respectively. For $w_{h-PB} = 0.8$, the DSC cooling curve in Figure 4 indicated that about 27% of crystallinty can be developed at the normal undercooling (due to the minor presence of lamellae with extended connectivity); therefore, this sample was annealed at room temperature for 2 h to allow completion of the crystallization associated with the normal undercooling prior to the low-temperature (−16 °C) crystallization experiment. It can be seen from Figure 6 that the crystallinity developments of both compositions are no longer sigmoidal; alternatively, the plots are properly described by eq 1, as also manifested from the linearities in the corresponding ln$[1 - x_c(t)]$ vs t plots.

The kinetics study reveals that crystallizations in the present dry-brush blend may be templated or confined depending upon the composition of h-PB. Long-range crystal growth was accessible to the neat PEO-*b*-PB and the blends with $w_{h-PB} < 0.8$ due to extensive connectivity of PEO lamellae templated by the melt morphology. Templated crystallization persisted until w_{h-PB} reached 0.8 where most PEO microdomains formed walls of spherical vesicles. The corresponding crystallization was effectively confined within the vesicle walls, and the exceedingly large number density of PEO domains led to a homogeneous nucleation-controlled crystallization. In general, the confinement effect exerted by dry-brush blending was far less effective than the corresponding wet-brush blending in which the confinement started to operate at $w_{h-PB} \approx 0.48$ (i.e., the composition where the PEO domains transformed into cylinders).[20,21]

Crystalline Morphology Generated through Rapid Quench to Low T_c. Most compositions of the present system ($w_{h-PB} < 0.8$) can crystallize at the normal undercooling owing to the templated mechanisms. Their crystallization windows thus cover the temperatures ranging from T_g^{PEO} (ca. −60 °C) to T_m^{PEO} (ca. 60 °C). Here we reveal a subtle difference between the crystalline morphology formed by crystallization at $T_c = 27$ °C and that generated through rapid quench from melt to liquid nitrogen. PEO is expected to crystallize very rapidly in the later process. Figure 7 shows the Lorentz-corrected SAXS profiles of the blends crystallized at 27 °C. The corresponding real-space morphology had been presented in Figure 3. It can be seen that the original scattering features associated with the melt structure (shown in Figure 1) smear out after the crystallization, where the lattice or form factor maxima are replaced by monotonically decayed profiles irrespective of compositions.

Figure 8 displays the TEM micrographs of neat PEO-*b*-PB and the blend with $w_{h-PB} = 0.2$ crystallized

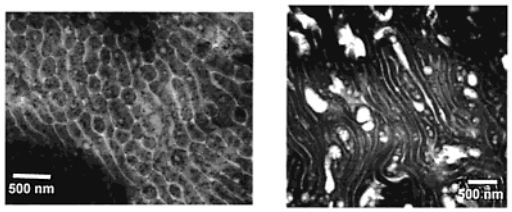

Figure 8. TEM micrographs showing the morphology of (a) neat PEO-*b*-PB and (b) the blend ($w_{h-PB} = 0.2$) crystallized through rapid quench from melt to liquid nitrogen. Neat diblock still exhibits perforated lamellar structure whereas the blend shows bended lamellar stacks.

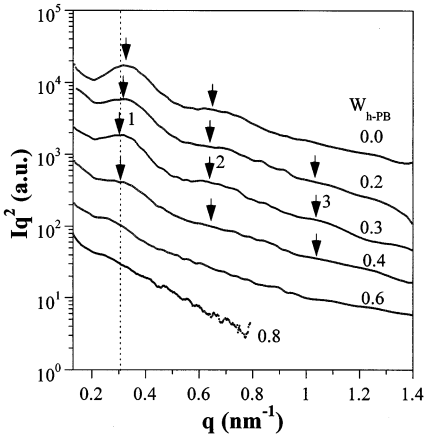

Figure 9. Lorentz-corrected SAXS profiles of dry-brush PEO-*b*-PB/h-PB blends crystallized by quench into liquid nitrogen. The blends with $w_{h-PB} \leq 0.6$ show scattering maxima with relative positions closely follow the ratio of 1:2:3.

through the quench process. The morphology observed by TEM is not much different from that generated through crystallization at 27 °C, where the neat diblock exhibits perforated lamellar structure and the blend shows bended lamellar stacks.

Although the TEM micrograph reveals similar morphological structure, the subtle difference between the crystalline morphology formed by the two crystallization conditions can be resolved by SAXS. Figure 9 displays the Lorentz-corrected SAXS profiles of the samples subjected to quench crystallization. In contrast to the profiles shown in Figure 7, broad maxima are identified in the scattering patterns up to $w_{h-PB} = 0.6$. The positions of these maxima are independent of composition, which seems to imply that the scattering feature is associated with the form factor of individual PEO domain. However, the observed profiles cannot be fitted by either lamellar or other types of form factors (including cylinder, sphere, and disk), because separation between the successive maxima is too large. As a matter of fact, the relative positions of these maxima closely follow the ratio of 1:2:3.., reminiscent of the lattice scattering from 1-D stacked lamellae. We thus propose the scattering feature to stem from the coherent correlation among the crystallites within individual PEO lamellar domains, as depicted schematically in Figure 10. Since PEO blocks crystallized at very deep undercooling during the quench, the high nucleation density could generate a great number of crystallites within each lamellar domains. These crystallites stacked into an imperfect 1-D lattice with the uncrystalline portion sandwiched between the crystallites, thereby yielding an alternating crystalline−amorphous layer structure

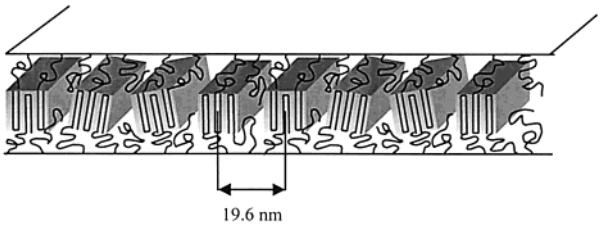

Figure 10. Schematic plot illustrating the highly polycrystalline structure in the individual PEO lamellae. The structure was characterized by two length scales, the first being the interlamellar distance of PEO microdomains intervened by the PB phase, and the other (ca. 19.6 nm) being the intercrystallite distance within the individual PEO domains.

similar to that found in the semicrystalline homopolymers. On the basis of this model, the intercrystallite distance calculated from the primary maximum in Figure 9 is 19.6 nm, and it is independent of w_{h-PB} because of identical crystallization condition. Consequently, a crystalline morphology characterized by two length scales is likely generated by the quench process—the first being the interlamellar distance of PEO microdomains intervened by the PB phase and the other being the intercrystallite distance within the individual PEO domains.

It can be seen from Figure 9 that the scattering maxima tend to diminish with increasing w_{h-PB} and disappear at $w_{h-PB} = 0.8$ where the system forms spherical vesicles. In this case, regular stacking of crystallites cannot be established within the vesicle walls owing to the small size and large interfacial curvature of the spherical vesicles.

Conclusions

The crystallization behavior in a dry-brush PEO-*b*-PB/h-PB blend system has been investigated over a broad composition range. In the melt state, the lamellar identity of PEO microdomains retained, but the lamellar units tended to form cylindrical or spherical vesicles at high w_{h-PB}. The crystallization mode in the system could be templated or confined depending upon w_{h-PB}. In neat PEO-*b*-PB and the blends with $w_{h-PB} < 0.8$, long-range crystal growth occurred through extensive connectivity of PEO lamellae templated by the melt morphology. Confined crystallization occurred at very high h-PB composition ($w_{h-PB} \geq 0.8$), where most PEO lamellae formed the walls of spherical vesicles. Crystallization in this case took place at very deep undercooling, and the corresponding crystallinity development during isothermal crystallization followed the first-order kinetics, indicating a homogeneous nucleation-controlled process. A highly polycrystalline structure was suggested to be formed within the individual PEO domains at $w_{h-PB} \leq 0.6$ when the crystallization was conducted through a rapid quench into liquid nitrogen. The crystalline morphology in this case was characterized by two length scales—the first being the interlamellar distance of PEO microdomains intervened by the PB phase and the other being the intercrystallite distance within the individual PEO domains.

Acknowledgment. This work was supported by the National Science Council of R.O.C. under Grant NSC 89-2216-E-007-048 and also in part by the US Department of Energy under Contract DE-AC05-00OR22725

with the Oak Ridge National Laboratory, managed by the UT-Battelle, LLC.

References and Notes

(1) Douzinas, K. C.; Cohen, R. E. *Macromolecules* **1992**, *25*, 5030.
(2) Cohen, R. E.; Bellare, A.; Drzewinski, M. A. *Macromolecules* **1994**, *27*, 2321.
(3) Hamley, I. W.; Fairclough, J. P. A.; Terrill, N. J.; Ryan, A. J.; Lipic, P. M.; Bates, F. S.; Towns-Andrews, E. *Macromolecules* **1996**, *29*, 8835.
(4) Hamley, I. W.; Fairclough, J. P. A.; Ryan, A. J.; Bates, F. S.; Towns-Andrews, E. *Polymer* **1996**, *37*, 4425.
(5) Quiram, D. J.; Register, R. A.; Marchand, G. R.; Adamson, D. H.; *Macromolecules* **1998**, *31*, 4891.
(6) Zhu, L.; Cheng, S. Z. D.; Calhoun, B. H.; Ge, Q.; Quirk, R. P.; Thomas, E. L.; Hsiao, B. S.; Yeh, F,-J.; Lotz, B. *J. Am. Chem. Soc.* **2000**, *122*, 5957.
(7) Zhu, L.; Cheng, S. Z. D.; Calhoun, B. H.; Ge, Q.; Quirk, R. P.; Thomas, E. L.; Hsiao, B. S.; Yen, F.; Lotz, B. *Polymer* **2001**, *42*, 5829.
(8) Zhu, L.; Cheng, S. Z. D.; Huang, P.; Ge, Q.; Quirk, R. P.; Thomas, E. L.; Lotz, B.; Hsiao, B. S.; Yeh, F.; Liu, L. *Adv. Mater.* **2002**, *14*, 31.
(9) Zhu, L.; Huang, P.; Chen, W. Y.; Ge, Q.; Quirk, R. P.; Cheng, S. Z. D.; Thomas, E. L.; Lotz, B.; Hsiao, B. S.; Yeh, F.; Liu, L. *Macromolecules* **2002**, *35*, 3553.
(10) Lotz, B.; Kovacs, A. J. *ACS Polym. Prepr* **1969**, *10*, 820.
(11) Robitaille, C.; Prud'homme, J. *Macromolecules* **1983**, *16*, 665.
(12) Nojima, S.; Nakano, H.; Ashida, T. *Polymer* **1993**, *34*, 4168.
(13) Nojima, S.; Nakano, H.; Takahashi, Y.; Ashida, T. *Polymer* **1994**, *35*, 3479.
(14) Nojima, S.; Yamamoto, S.; Ashida, T. *Polym. J.* **1995**, *27*, 673.
(15) Ryan, A. J.; Hamley, I. W.; Bras, W.; Bates, F. S. *Macromolecules* **1995**, *28*, 3860.
(16) Schnablegger, H.; Rein, D. H.; Rempp, P.; Cohen, R. E. *J. Polym. Eng.* **1996**, *16*, 1.
(17) Hamley, I. W.; Fairclough, J. P. A.; Bates, F. S.; Ryan, A. J. *Polymer* **1998**, *39*, 1429.
(18) Weimann, P. A.; Hajduk, D. A.; Chu, C.; Chaffin, K. A.; Brodil, J. C.; Bates, F. S. *J. Polym. Sci., Polym. Phys. Ed.* **1999**, *37*, 2053.
(19) Loo, Y.-L.; Register, R. A.; Ryan, A. J. *Phys. Rev. Lett.* **2000**, *84*, 4120.
(20) Chen, H. L.; Hsiao, S. C.; Lin, T. L.; Yamauchi, K.; Hasegawa, H.; Hashimoto, T. *Macromolecules* **2001**, *34*, 671.
(21) Chen, H. L.; Wu, J. C.; Lin, T. L.; Lin, J. S. *Macromolecules* **2001**, *34*, 6936.
(22) Zhu, L.; Mimnaugh, B. R.; Ge, Q.; Quirk, R. P.; Cheng, S. Z. D.; Thomas, E. L.; Lotz, B.; Hsiao, B. S.; Yeh, F.; Liu, L. *Polymer* **2001**, *42*, 9121.
(23) Loo, Y.-L.; Register, R. A.; Ryan, A. J.; Dee, G. T. *Macromolecules* **2001**, *34*, 8968.
(24) Loo, Y.-L.; Register, R. A.; Ryan, A. J. *Macromolecules* **2002**, *35*, 2365.
(25) Müller, A. J.; Balsamo, V.; Arnal, M. L.; Jakob, T.; Schmalz, H.; Abetz, V. *Macromolecules* **2002**, *35*, 3048.
(26) Xu, J. T.; Turner, S. C.; Fairclough, J. P. A.; Mai, S. M.; Ryan, A. J. *Macromolecules* **2002**, *35*, 3614.
(27) Lee, W.; Chen, H.-L.; Lin, T.-L. *J. Polym. Sci., Polym. Phys. Ed.* **2002**, *40*, 519.
(28) Cohen, R. E.; Cheng, P. L.; Douzinas, K.; Kofinas, P.; Berney, C. V. *Macromolecules* **1990**, *23*, 324.
(29) Nojima, S.; Kato, K.; Yamamoto, S.; Ashida, T. *Macromolecules* **1992**, *25*, 2237.
(30) Zhu, L.; Chen, Y.; Zhang, A.; Calhoun, B. H.; Chun, M.; Quirk, R. P.; Cheng, S. Z. D.; Hsiao, B. S.; Yeh, F.; Hashimoto, T. *Phys. Rev. B* **1999**, *60*, 10022.
(31) Loo, Y.-L.; Register, R. A.; Adamson, D. H. *J. Polym. Sci., Polym. Phys. Ed.* **2000**, *38*, 2564.
(32) Chen, H.-L.; Li, H.-C.; Huang, Y.-Y.; Chiu, F.-C. *Macromolecules* **2002**, *35*, 2417.
(33) Sakurai, K.; MacKnight, W. J.; Lohse, D. J.; Schultz, D. N.; Sissano, J. A. *Macromolecules* **1994**, *27*, 4941.
(34) Rangarajan, P.; Register, R. A.; Fetters, L. J.; Bras, W.; Naylor, S.; Ryan, A. J. *Macromolecules* **1995**, *28*, 4932.
(35) Quiram, D. J.; Register, R. A.; Marchand, G. R. *Macromolecules* **1997**, *30*, 4551.
(36) Quiram, D. J.; Register, R. A.; Marchand, G. R.; Ryan, A. J. *Macromolecules* **1997**, *30*, 8338.
(37) Nojima, S.; Tanaka, H.; Rohadi, A.; Sasaki, S. *Polymer* **1998**, *39*, 1727.
(38) Hong, S.; Yang, L.; MacKnight, W. J.; Gido, S. P. *Macromolecules* **2001**, *34*, 7009.
(39) Hashimoto, T.; Tanaka, H.; Hasegawa, H. *Macromolecules* **1990**, *23*, 4378.
(40) Tanaka, H.; Hasegawa, H.; Hashimoto, T. *Macromolecules* **1991**, *24*, 240.
(41) Winey, K. I.; Thomas, E. L.; Fetters, L. J. *Macromolecules* **1992**, *25*, 2645.
(42) Koizumi, S.; Hasegawa, H.; Hashimoto, T. *Makromol. Chem. Macromol. Symp.* **1992**, *62*, 75.
(43) Hashimoto, T.; Koizumi, S.; Hasegawa, H. *Physica B* **1995**, *213*, 679.
(44) Kinning, D. J.; Winey, K. I.; Thomas, E. L. *Macromolecules* **1988**, *21*, 3502.
(45) Khandpur, A. K.; Forster, S.; Bates, F. S.; Hamley, I. W.; Ryan, A. J.; Bras, W.; Almdal, K.; Mortensen, K. *Macromolecules* **1995**, *28*, 8796.
(46) Qi, S.; Wang, Z.-G. *Phys. Rev. E* **1997**, *55*, 1682.
(47) Avrami, M. *J. Chem. Phys.* **1939**, *7*, 1103.

MA020997L